Chapter 5

MHD model flows with shocks: characteristic analysis and grid convergence study

In this Chapter we present five model flows of increasing complexity belonging to the class of stationary 2D planar field-aligned MHD flows. The purpose of this Chapter is two-fold. First, we analyze the physical properties of these five flows using characteristic theory. This illustrates the characteristic theory derived in Chap. 3 and how this theory can be used to interpret MHD flows. Second, we derive grid convergence criteria for flows belonging to this class from characteristic theory, and grid convergence is demonstrated for the numerical simulation of the five model flows with our numerical MHD code using the Lax-Friedrichs scheme. It is investigated, by formal grid convergence studies of magnetic flux conservation and other flow quantities, whether the Powell source term approach to control the $\nabla \cdot \vec{B}$ constraint leads to correct results for this class of flows. This grid convergence study is important because it constitutes the validation of the numerical technique used in this dissertation. In the Appendix a model flow is presented which is not field-aligned, and it is discussed how grid convergence can be studied for this flow.

The main content of this Chapter will appear in [148].

5.1 Introduction

We present five field-aligned model flows, with increasing complexity in terms of wave features present in the flow: a fully smooth radial outflow, an expanding tube flow with a weak discontinuity, a wedge flow with a plane fast shock, a bow shock flow with a curved fast shock, and a nozzle flow with reflecting fast shocks. These model flows describe various nonlinear wave phenomena in their most basic form. The corresponding Euler flows have been described and used many times, but in the numerical MHD literature these basic flows have not received much attention yet. We show that this set of model problems is well suited to test grid convergence of MHD codes, and to study in detail how the behavior of numerical schemes changes when increasingly complex wave structures are present in the flow. Characteristic analysis reveals basic invariants of the flow, and these invariants can be used to test grid convergence as they lead to analytical solutions for some combinations of the flow variables if the incoming flow is uniform. Characteristic analysis also provides a clear insight into the physical properties of the model flows and into the stationary wave features present in the flows.

Although these five model problems exhibit quite a variety of flow features, they all belong to the sub-class of stationary planar 2D field-aligned MHD flows. Stationary flow has important applications [159, 55, 56, 150, 93, 53, 100] and any stationary 2D problem where ideal wall boundary conditions are present automatically leads to a solution where the magnetic field is aligned to the velocity field in the whole simulation domain. Hence the class of stationary field-aligned flow is an important class of MHD flows. One could even argue that 2D stationary flow problems in a finite domain with the magnetic field *not* aligned to the plasma flow are rare [61, 93, 53]. It is hard to define the boundary conditions consistently in that case. However, it is important to test MHD codes also for non-field-aligned flow. Therefore we include one model problem for which the magnetic field is not aligned to the plasma flow. This model flow is constructed in a special way; the fields are actually aligned in a rotating frame, but not in the rest frame. The analysis of this model problem is substantially different from the analysis of the field-aligned problems, so we prefer to present and analyze this non-field-aligned flow problem in an Appendix, while the grid convergence results for this flow are integrated in the discussion in the main text.

Although most model problems presented in the MHD literature only allow for qualitative comparison and cannot be used for formal accuracy testing, a very limited number of (mostly 1D) test problems have been described which allow for some degree of formal accuracy testing. Stone et al. [157, 158] present 1D model problems including stellar wind flows and obtain grid convergence which is satisfactory for most cases. Ryu et

al. [129] show that the numerical dissipation of their scheme vanishes in second order as a function of grid resolution. Vanden Abeele and Deconinck [1] show how the conservation of magnetic flux in a flux tube can be used as a measure of improved accuracy as a function of grid resolution. Barth [7] obtains 'optimal' grid convergence for the $\nabla \cdot \vec{B}$ constraint in a continuous Prandtl-Meyer flow with an added magnetic field. The most interesting approach to grid convergence studies of MHD codes to date can probably be found in Linde's PhD thesis [99]. This author describes briefly a wedge flow and a stellar wind flow, and obtains satisfactory grid convergence. Although we have made use of some of the ideas presented in the above cited articles, the variety of problems presented in this Chapter, and especially the firm grounding of convergence study on the rigorous and complete characteristic analysis of the model flows, are new in the grid convergence study of MHD codes.

The numerical enforcement of the $\nabla \cdot \vec{B}$ constraint is an important and much debated problem for numerical MHD codes. In Chap. 4 a new approach to control $\nabla \cdot \vec{B}$ presented by Powell [118] has been described. In this Chapter we employ the Powell source term technique and we investigate by formal grid convergence studies of magnetic flux conservation and other flow quantities, if this approach is valid, at least for the class of stationary flow problems that we consider. Linde [99] and Barth [7] carry out a similar study and confirm the validity of the Powell source term approach, but their investigation is less complete and systematic than ours, and is carried out on adaptively refined Cartesian grids [99] or on unstructured grids [7], and not on the body-fitted structured grids used in our numerical approach.

In the next Section we present the five field-aligned model flows and their analysis in terms of stationary characteristics. In Sec. 5.3 we discuss grid convergence criteria. Sec. 5.4 contains the results of the grid convergence study of the five field-aligned model flows and one non-field-aligned model flow, which is presented and analyzed in the Appendix.

5.2 Characteristic analysis of model flows

5.2.1 Cylindrical expansion flow

The first model flow (Fig. 5.1) is a stationary cylindrical expansion flow in the domain ($r \in [1,2]$, $\theta \in [0°, 30°]$) with planar symmetry ($\partial/\partial z \equiv 0$). All the figures shown in this Section represent simulation results obtained with our numerical MHD code using a second order Lax-Friedrichs scheme. In Fig. 5.1, a uniform superfast inflow with radial magnetic field is imposed at the $r = 1$ boundary, with $\rho = 1$, $p = 1$, $v_r = 3$ and $B_r = 1$. The sonic and Alfvénic inflow Mach numbers are thus $M = 3\sqrt{3}/\sqrt{5}$ and $M_A = 3$. The plasma is allowed to flow out freely at $r = 2$. For

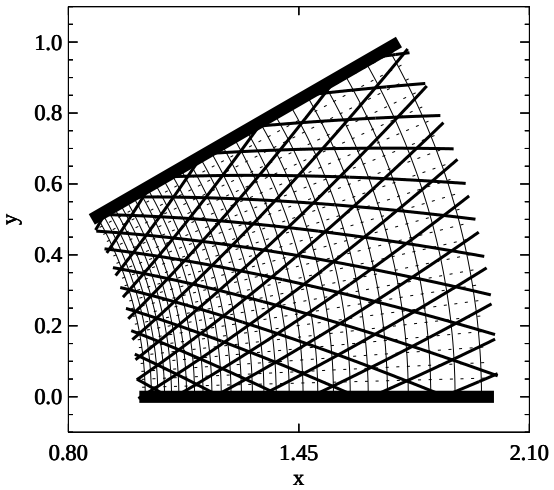

Figure 5.1: *The cylindrical expansion flow (70 × 70 grid). Density contours (thin solid) and streamlines (thin dotted) are shown. The streamlines are also magnetic field lines. The thick solid lines represent simulation domain boundaries with ideal wall symmetry. The flow is hyperbolic in the whole simulation domain. Two families of fast characteristics (thick solid) make equal angles with the streamlines. The flow is smooth in the whole simulation domain.*

$r > 1$, a stationary completely smooth radial expansion profile with variables only changing as a function of r results. This flow is thus strictly speaking a 1D flow.

In Fig. 5.1 and the subsequent figures, density contours are shown as thin solid lines, and streamlines as thin dotted lines. The streamlines are also magnetic field lines. The streamlines are threefold-degenerate characteristics with s, h_s and ρ/α as associated RIs. The thick solid lines represent simulation domain boundaries with ideal wall symmetry. Two families of fast characteristics (thick solid) make equal angles with the streamlines in hyperbolic regions.

As the inflow in Fig. 5.1 is uniform and every streamline thus carries the same values for the RIs s, h_s and ρ/α, those RIs are global invariants over the whole flow domain. $\nabla \cdot \vec{B} = 0$ and $B_r(1) = 1$ imply that $B_r(r) = 1/r$. The four state variables ρ, p, B_r and v_r can thus be determined as a function of r from $B_r(r) = 1/r$ and the three global invariants, which establishes the exact analytical solution of this flow problem. The flow

is hyperbolic Hf1 (Fig. 3.4) everywhere, so the two (generalized) Mach characteristics exist. This flow is smooth everywhere, and this is the property which distinguishes it from the model flows to be presented next, which contain increasingly complex (weakly) discontinuous flow features. This flow is related to the stellar outflow problems discussed in [131, 157, 158, 99, 82]. By giving the flow a rotational component at the inflow boundary, we obtain a non-field-aligned model problem describing radial outflow from a rotating object [131, 82]. This rotating outflow problem is described and analyzed in the Appendix.

5.2.2 Expanding tube flow

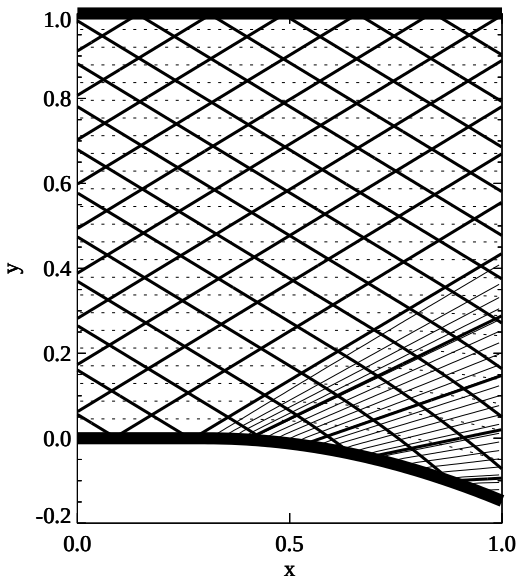

Figure 5.2: *The expanding tube flow (75 × 125 grid). The flow is hyperbolic in the whole simulation domain. A weak discontinuity detaches from the lower wall where the tube starts to expand. This weak discontinuity is a fast characteristic, and is followed by a simple wave rarefaction region. One family of characteristics consists of straight lines in the simple wave region. The simple wave is not centered.*

In Fig. 5.2 we show a stationary expanding tube flow in the domain ($x \in [0,1]$, $y \in [y_0(x),1]$), with $y_0(x) = 0$ for $x \in [0,0.3]$ and $y_0(x) = -1 + \cos(\pi/4 * (x-0.3))$ for $x \in [0.3,1]$. A uniform superfast horizontal inflow with horizontal magnetic field is imposed at the $x = 0$ boundary, with $\rho = 1$, $p = 1$, $v_x = 8$ and $B_x = 4$. The sonic and Alfvénic inflow Mach numbers are thus $M = 8\sqrt{3}/\sqrt{5}$ and $M_A = 2$. The plasma is allowed to flow out freely at $x = 1$, where the flow remains superfast. At $y = y_0(x)$ and $y = 1$ we impose ideal wall symmetry conditions. A stationary expanding flow results, as shown by the density contours of Fig. 5.2.

The flow is hyperbolic Hf2 (Fig. 3.4) in the whole simulation domain, such that two families of fast characteristics exist. As long as the lower wall is straight, the flow is uniform. When the wall starts to curve ($x = 0.3$), this acts as a (wave-like) perturbation, which can only propagate downstream along the characteristics. This means that the flow is non-uniform only below the upward fast characteristic which originates from the lower boundary at ($x = 0.3$) with an angle of $\theta = 31.276°$, as can be calculated from Eq. (3.68). This fast characteristic thus separates a uniform flow region from a perturbed region, and is thus necessarily a *weak discontinuity* [20, 21]. At a weak discontinuity, the spatial derivative of the flow variables in a direction perpendicular to the weak discontinuity characteristic, is discontinuous. However, the flow variables themselves are continuous, and the entropy is thus also conserved on streamlines across weak discontinuities. A weak discontinuity thus detaches from the lower wall where the tube starts to expand.

This weak discontinuity is followed by a simple wave [20, 21, 151] rarefaction region. This rarefaction is called a (stationary) simple wave because it carries a variation in only one MHD wave family. It is a property of simple waves that one family of characteristics consists of straight lines, and that the flow variables are constant along these characteristics, which makes the characteristics parallel to the contour lines of flow variables, e. g. the density, as can be seen in Fig. 5.2. In the present flow, these straight line characteristics do not converge in one point, so this simple wave is not centered. Centered simple waves exist in rarefaction flows around sharp corners, like the well-known Prandtl-Meyer flow [7]. Such a sharp corner is a geometrical singularity in the boundary and this can complicate grid convergence studies, as is explained in the next Section. For this reason, we have chosen to present model flows with smooth boundaries in this Chapter. A simple wave, also if it is non-centered, can be described mathematically as a function of only one spatial parameter, so strictly speaking this flow is 1D. As the inflow is uniform, every streamline throughout the whole domain carries the same values for RIs h_s and ρ/α, and also for s as the flow does not contain strong discontinuities. These RIs are thus global invariants over

the whole flow domain.

This flow contains a weak discontinuity, and this is the property which distinguishes it from the fully smooth model flow discussed in Sec. 5.2.1.

5.2.3 Wedge flow

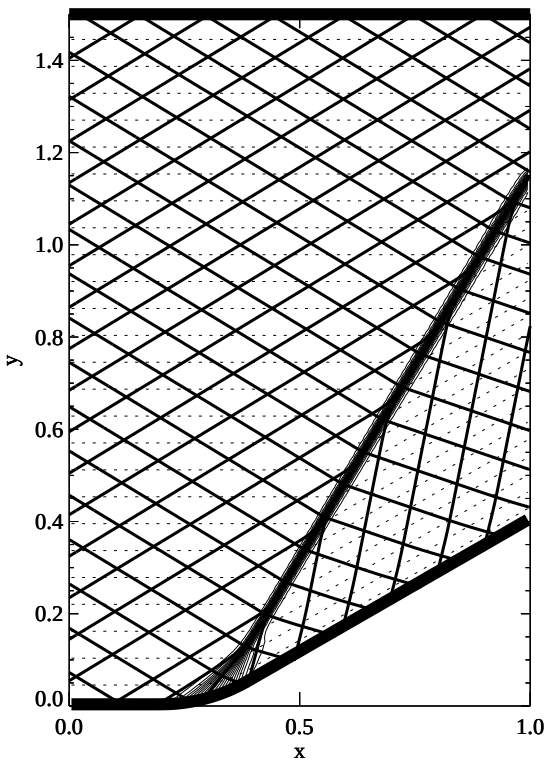

Figure 5.3: *The wedge flow (*100×200 *grid). The flow is hyperbolic in the whole simulation domain. A plane fast MHD shock is formed where characteristics start to intersect near the lower wall. This discontinuity stretches out upwards in a straight line.*

In Fig. 5.3 we show a stationary wedge flow in the domain ($x \in [0, 1]$,

$y \in [y_0(x), 1.5]$). The lower simulation domain boundary has the form of a wedge with angle $\theta = 30°$.

A uniform superfast horizontal inflow with horizontal magnetic field is imposed at the $x = 0$ boundary, with $\rho = 1$, $p = 1$, $v_x = 8$ and $B_x = 4$. The sonic and Alfvénic inflow Mach numbers are thus $M = 8\sqrt{3}/\sqrt{5}$ and $M_A = 2$. At $y = y_0(x)$ and $y = 1$ we impose ideal wall symmetry conditions. The wedge geometry causes the formation of a fast MHD shock, as shown by the accumulation of density contours in a solid line. At the shock, the magnetic field lines are refracted away from the shock normal in going from upstream to downstream, which shows that this is a fast MHD shock. The plasma is allowed to flow out freely at $x = 1$, where the (normal) flow is superfast.

As the inflow is uniform, every streamline throughout the whole domain carries the same values for h_s and ρ/α, but not for s since the flow does contain a strong discontinuity where the entropy increases discontinuously. Only the RIs h_s and ρ/α are thus global invariants over the whole flow domain. The flow is hyperbolic Hf2 (Fig. 3.4) everywhere, so the two (generalized) Mach characteristics exist.

We have to remark that the two straight 'legs' of the wedge could be connected at $x = 0.3$, but that we have again chosen for a smooth boundary with the wedge corner smoothed out by a circular profile. The lower boundary is described by $y_0(x) = 0$ for $x \in [0, 0.2]$ and $y_0(x) = \tan(30°) * (x - 0.3)$ for $x \in [0.3 + 0.1 * \cos(30°), 1]$. A segment of a circle with center point $(0.2, 0.1 * (1 + \cos(30°))/\sin(30°))$ and radius $r = 0.1 * (1 + \cos(30°))/\sin(30°)$, which is tangent to the two 'legs' of the wedge, then replaces the corner singularity of the wedge with a smooth profile. Close to the lower boundary our wedge flow with smooth boundaries is thus slightly different from a wedge flow with a sharp corner, and one can see a small compressional wave region with converging characteristics in the corner region on Fig. 5.3 [160], but above the point where those characteristics converge and the shock is formed, this flow is identical to the wedge flow with a sharp corner.

The wedge flow described in this Section contains a plane strong discontinuity, and this is the property which distinguishes it from the flows discussed earlier. MHD wedge flows have also been discussed in [99].

5.2.4 Bow shock flow

In Fig. 5.4 we show a stationary bow shock flow in the domain ($r \in [r_0(\theta), 0.125]$, $\theta \in [90°, 180°]$), with $r_0(\theta) = 0.75 - 0.45\,(\theta - 90)/90$. The bow shock is formed by the obstruction of a uniform incoming flow by a rigid perfectly conducting circular cylinder with $r = 0.125$. A uniform superfast horizontal inflow with horizontal magnetic field is imposed at

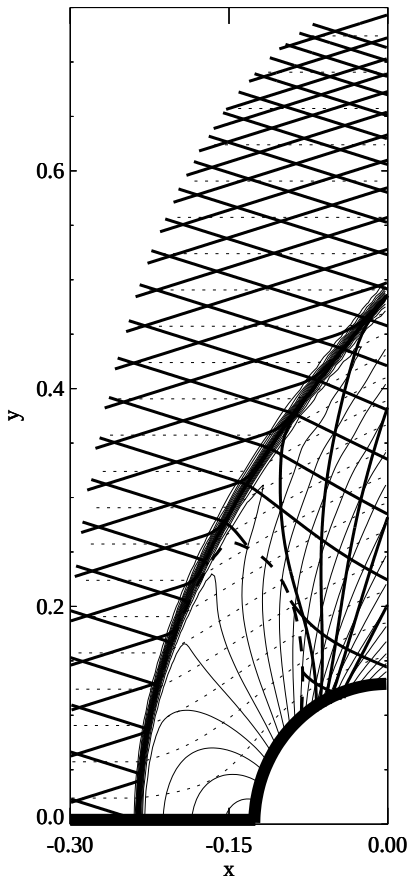

Figure 5.4: *The bow shock flow (80 × 80 grid). A fast MHD bow shock is formed in front of the cylindrical obstacle. The flow is hyperbolic in front of this bow shock, and also behind the shock front sufficiently far upward from the horizontal x-axis. The region behind the shock front and close to the horizontal x-axis, is an elliptic region, in which real fast characteristics do not exist. This elliptic region is separated from the upward hyperbolic region by the $M = 1$ contour (dashed).*

the $r = r_0$ boundary with $\rho = 1$, $p = 0.2$, $v_x = 2$, and $B_x = 0.1$. The sonic and Alfvénic inflow Mach numbers are thus $M = 2\sqrt{3}$ and $M_A = 20$. At $y = 0$ and $r = 0.125$ we impose ideal wall symmetry conditions. The plasma is allowed to flow out freely at $x = 0$, where the (normal) flow is superfast. A curved fast MHD bow shock is formed,

as shown by the accumulation of density contours. At the shock, the magnetic field lines are refracted away from the shock normal in going from upstream to downstream, which shows that this is a fast MHD shock.

As the inflow is uniform, every streamline throughout the whole domain carries the same values for h_s and ρ/α, but not for s as the flow does contain a strong discontinuity. Only the RIs h_s and ρ/α are thus global invariants over the whole flow domain. The flow is hyperbolic Hf1 (Fig. 3.4) in the upstream region and in the part of the downstream region above the dashed line (the $v^2 = c^2$ or $M = 1$ contour). In these hyperbolic regions the two (generalized) Mach characteristics exist. The downstream region below the $M = 1$ contour is of elliptic type Efs1, and real characteristics do not exist in this region.

The bow shock flow described in this Section contains a curved strong discontinuity and an elliptic region, and these properties distinguish it from the flows discussed earlier. MHD bow shock flows have been discussed before in [1, 150, 161, 7, 151]. In Chap. 6 we describe the characteristic analysis of a complex MHD bow shock flow which contains interacting fast and intermediate shocks and tangential discontinuities, and several alternating regions of the different hyperbolic and elliptic types of Fig. 3.4.

5.2.5 Nozzle flow

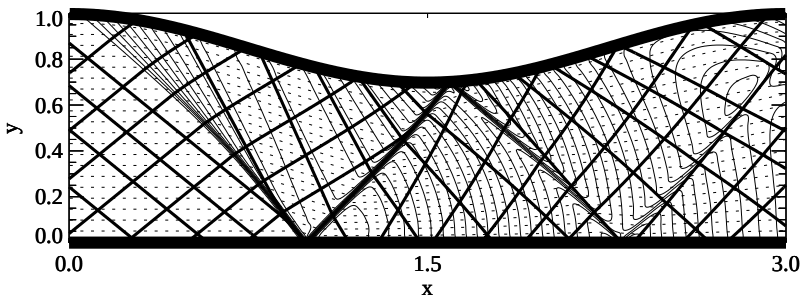

Figure 5.5: *The nozzle flow (480 × 160 grid). The flow is hyperbolic in the whole simulation domain. A fast MHD shock is formed where characteristics start to intersect. This shock is reflected by the lower wall, by the upper wall, and again by the lower wall, before it leaves the simulation domain. Throughout these reflections, the shock front remains nearly plane and the shock remains of the fast type.*

In Fig. 5.5 we show a stationary nozzle flow in the domain ($x \in [0,3]$, $y \in [0, y_1(x)]$), with $y_1(x) = 1 - 0.3 * \sin^2(\pi/3 * x)$. A uniform superfast horizontal inflow with horizontal magnetic field is imposed at the $x = 0$ boundary with $\rho = 1$, $p = 1$, $v_x = 3.5$, and $B_x = 2$. The sonic and Alfvénic inflow Mach numbers are thus $M = 3.5\sqrt{3}/\sqrt{5}$ and $M_A = 1.75$. At $y = 0$ and $y = y_1$ we impose ideal wall symmetry conditions. The plasma is allowed to flow out freely at $x = 3$, where the (normal) flow is superfast. A fast MHD shock is formed near the upper wall because of the curvature of this wall, as shown by the accumulation of density contours. At the shock, the magnetic field lines are refracted away from the shock normal in going from upstream to downstream, which shows that this is a fast MHD shock. This shock reflects several times from the rigid ideal walls $y = 0$ and $y = y_1(x)$.

As the inflow is uniform, every streamline throughout the whole domain carries the same values for h_s and ρ/α, but not for s as the flow does contain strong discontinuities. Only the RIs h_s and ρ/α are thus global invariants over the whole flow domain. The flow is hyperbolic Hf2 (Fig. 3.4) everywhere, and two (generalized) Mach characteristics exist.

The nozzle flow described in this Section contains strong discontinuities which are reflected by ideal walls, which distinguishes it from the flows discussed earlier. MHD nozzle flows have been discussed before in [1].

5.3 Grid convergence criteria

In this Section we define grid convergence criteria for stationary model flows, but first we discuss what kind of convergence order we can expect for model flows simulated with the numerical techniques discussed in Chap. 4.

Formal grid convergence

The basic idea of grid convergence is that for smooth flow (see below), some measure of the error of the simulation result should decrease as a function of the resolution with an order which is the formal order of accuracy of the scheme. Formal Taylor series expansion of the numerical schemes presented in Chap. 4 would show that for a stationary solution

$$E = ||\mathbf{U} - \overline{\mathbf{U}}|| = c\ (1/n)^p, \tag{5.1}$$

with $\mathbf{U}$ the exact solution, $\overline{\mathbf{U}}$ the numerical solution, E the error in some norm, c a constant, n the number of cells in a certain direction — where it is understood that the resolution is changed proportionally in all directions —, and p the order of the method (1 or 2 for the schemes

discussed in Chap. 4). On logarithmic axes this would lead to grid convergence curves which are straight lines with slope 1 or 2

$$\log(E) = \log(c) - p\,\log(n). \tag{5.2}$$

All state variable quantities are expected to be calculated with the accuracy of the scheme. It is important to remark here, however, that the $\nabla \cdot \vec{B}$ quantity ('magnetic flux production per unit volume') with discretization given by Eq. 4.30, is a sum of derivatives of the magnetic field state variables, and can thus be expected to converge more slowly than the state variables, in the worst case with one order less [33, 7]. Probably for this reason, Linde [99] proposes to measure magnetic flux conservation in a different way. The following alternative quantity

$$F_{i,j} = \frac{\sum_{k=1}^{4} \vec{B}_k \cdot \vec{n}_k \, \Delta l_k}{\sum_{k=1}^{4} \Delta l_k}, \tag{5.3}$$

is a measure of magnetic flux conservation ('flux production per unit length') which should converge at least with the same order as the state variables. We investigate how these two measures of flux conservation behave for the numerical simulation of our five model flows.

The actually observed convergence order for a numerical simulation can be lower than the formal order of accuracy of the scheme because of several reasons. We discuss in short five possible reasons of convergence degradation. The first two reasons are related to the analytical properties of fluid flows, viz. to the *regularity* of flows. The latter three reasons for convergence degradation are more related to the details of the numerical scheme.

First, when the analytical solution to a flow contains (weak) discontinuities, then the derivatives in the above mentioned Taylor expansion do not exist everywhere, which means that the convergence order result derived using the Taylor expansion is not valid. In general it can be expected that the convergence order for a numerical scheme is lower for a solution containing discontinuities. Leveque [90] gives an example where the convergence order of an approximation degrades by 0.5 for a solution containing a discontinuity.

Second, near geometrically singular points on boundaries, the analytical solution to the flow problem is generally not smooth, with similar consequences of convergence order degradation [135]. These effects can be reduced by choosing smooth boundaries, as we have done for all our model flows, but even then the finite grid resolution leads to singular corners at curved boundaries. The effects of these singularities can be reduced by a careful geometrical refinement of the grid near the boundary [135]. Barth [7] reports improved grid convergence if interpolation at the boundary interfaces is done with higher order polynomials than

inside the domain (so-called *iso-parametric* boundaries), in the context of finite element methods which allow for more flexibility than our finite volume schemes.

Third, the choice of numerical flux function seems to be important for the errors induced at boundaries. For instance, it is well-known that the Roe scheme can lead to the problem of *wall-heating* at perfect wall boundaries [91]. It seems that our choice of the Lax-Friedrichs flux function in general performs better in such situations, and our grid convergence results seem generally to be satisfactory. We have thus not adopted the strategy to exclude physical cells close to the boundaries from our error norm calculations [157, 158], because we think that this process is somewhat artificial and arbitrary, and because we want to prove grid convergence of our numerical scheme with the boundary treatment included. We have to admit, however, that the errors are often large not only at discontinuities, but also at the boundaries.

Fourth, near discontinuities our second order scheme switches to first order accuracy due to the action of the nonlinear limiter. In error norms calculated over the whole simulation domain, these local first order errors dominate the second order errors in smooth parts of the flow, resulting in convergence degradation to first order.

Fifth, simulations on highly distorted grids, with angles in cells substantially deviating from 90° or with cells highly elongated, may show degraded convergence rates [164].

Practical grid convergence criteria

For the model flows we propose in this Chapter, the analytical solution is generally not known. How can we carry out grid convergence studies then? We do not engage in the use of 'self-convergence' criteria [157, 158], because they do not easily lead to rigorous conclusions.

But even when the analytical solution is not known, we can formulate grid convergence criteria. In general we can distinguish three classes of grid convergence criteria.

The first class of criteria follows directly from the divergence nature of the steady conservation law (Eq. 3.12 with vanishing time derivative) and the $\nabla \cdot \vec{B}$ constraint. These laws basically state that the divergence of a flux vanishes. This leads to grid convergence criteria in two ways.

First, over the whole physical domain, the integrated form of the divergence law shows that the line integral of the normal flux through the circumference of the physical domain has to vanish. For instance, in a steady flow the net flux of density (the momentum) through the boundaries has to vanish, and numerically this net flux has to converge to zero as a function of resolution. This, however, merely checks global conservation and only gives a very global measure of accuracy as internal

errors can cancel out. This grid convergence measure is not further exploited in this Chapter.

Second, when the flux vectors are aligned with a boundary at two opposing boundaries of the simulation domain, and the boundaries thus form *flux tubes*, then the flux through any line connecting the two boundaries has to be the same. This can be tested along lines consisting of cell interfaces. We use this observation extensively to verify if the magnetic and momentum fluxes through sections of flux tubes are constant along the flux tube. This leads to a more local measure of accuracy. Suppose for instance that the boundaries below $j = 1$ and above $j = n_j$ are perfect walls, then we can calculate the (magnetic or momentum) flux $\Phi_{i+1/2}$ through every line formed by interfaces between cells with equal coordinates i and $i+1$, using the reconstructed $\mathbf{U}_l$ and $\mathbf{U}_r$ in the average $(\mathbf{U}_l + \mathbf{U}_r)/2$ at every interface, and with i running from 0 to n_i. Then an L1 error measure can be defined as

$$E_\Phi^{B,m} = \frac{\sum_{i=0}^{i=n_i} \mathrm{abs}(\Phi_{i+1/2} - \Phi_{theor})}{n_i + 1} \tag{5.4}$$

with Φ_{theor} being the known theoretical value of the flux, and E_Φ^B and E_Φ^m the magnetic and momentum flux error measure respectively. Flux conservation criteria like this have been used before to investigate the accuracy of MHD simulations as a function of resolution [157, 158, 1, 99].

The second class of grid convergence criteria follows from the rigorously defined characteristic properties of the class of flows under consideration, and leads to measures of true local grid convergence in every cell of the simulated flow. There can be up to four global invariants for stationary planar field-aligned flow, as follows from characteristic analysis. The angle θ between the magnetic and the velocity fields has to vanish everywhere. In the case of uniform inflow, Riemann invariants ρ/α and h_s are global invariants. If the flow is additionally smooth, then Riemann invariant s is a fourth global invariant. An L1 error measure for these invariants I can be defined as

$$E_I = \frac{\sum_{i,j} \mathrm{abs}(\overline{I}_{i,j} - I_{theor})\, \Omega_{i,j}}{\sum_{i,j} \Omega_{i,j}} \tag{5.5}$$

with I_{theor} being the known theoretical value of the invariant. Note that we actually calculate the difference between the cell-averaged numerically calculated values of the invariant and the cell-average of the theoretical value of the invariant (which, of course, is the invariant itself). Global grid convergence criteria based on characteristic invariants have to our knowledge not been used before to investigate the accuracy of 2D MHD simulation results as a function of resolution. The s and h_s quantities keep their invariant properties in stationary Euler flow, so

this type of grid convergence study can also be carried out for that case, as is well-known. Finally, we should mention that $\nabla \cdot \vec{B}$ should vanish in theory for every MHD flow, so this can easily be tested using the same expression to calculate the error.

The third class of grid convergence criteria follows from the RH jump relations. If sufficient information is available in terms of imposed upstream flow conditions and geometrical constraints, then the remaining unknown values can be calculated from Eq. 3.75 with high accuracy, and in some cases analytical solutions can be found. These values can then be compared with the values resulting from full 2D numerical simulations of the flow, and grid convergence can be investigated.

In practice, we measure the simulation error using the above given expressions E as a function of the number of grid cells in a certain direction n, and determine the numerical convergence order by a least-squares fit of the $\log E$–$\log n$ curve with generally four data points.

5.4 Grid convergence study of model flows

In this Section we discuss numerical simulation aspects of the model flows presented in Sec. 5.2 and the non-field-aligned flow presented in the Appendix, and we present grid convergence results obtained with the criteria discussed in Sec. 5.3.

5.4.1 Numerical simulation aspects

The steady state simulation results shown in Figs. 5.1–5.5 were obtained via time-accurate relaxation starting from uniform initial states. Fig. 5.6 shows the convergence of the logarithm of the density residual $\overline{R}(m)$ (Eq. 4.49) towards a steady state in function of the number of time steps. We can observe that the steady state convergence of our numerical scheme is extremely well behaved. For all simulations we obtain convergence up to machine accuracy both using the first order scheme (solid) and the second order scheme (dash-dotted). The number of time steps needed to obtain convergence is mostly similar for the first and the second order schemes. We used the same CFL number for the first and the second order scheme. The computational cost per time step is, however, about three times higher for the second order scheme. The number of time steps is much higher for the bow shock flow than for the other flows, because of the low velocities in the elliptic region near the stagnation point.

Fig. 5.7 shows the simulation grids used for the numerical results presented in this Chapter. The grids are nearly uniform and the grid cells are mostly quite regular, except perhaps for some strongly deformed cells in the bow shock grid. For the cylindrical expansion problem and the

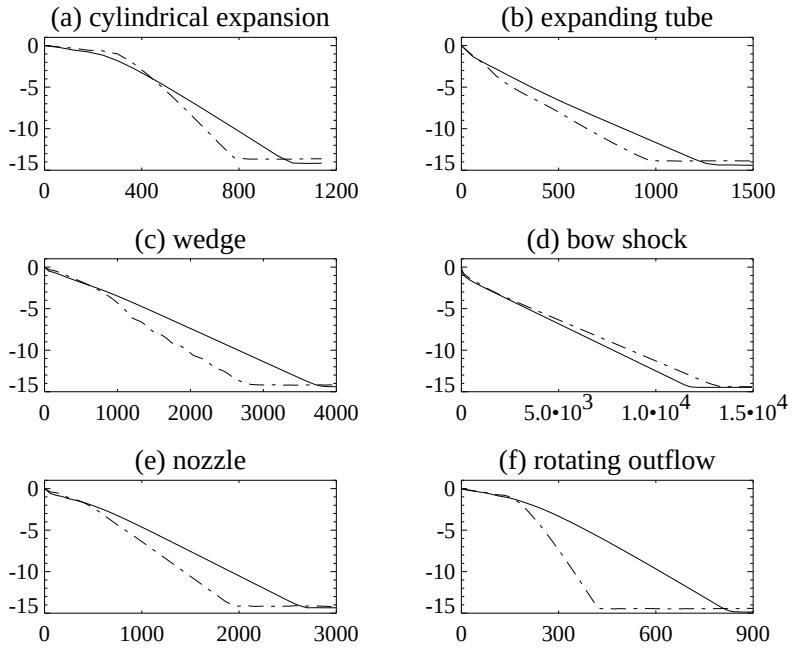

Figure 5.6: *Convergence of the logarithm of the density residual towards a steady state, as a function of the number of time steps. First order (solid) and second order (dash-dotted) numerical schemes.*

rotating outflow problem the grid convergence has been studied making use of simulations on 40×40, 50×50, 60×60 and 70×70 grids. The expanding tube problem has been simulated on 30×50, 45×75, 60×100 and 75×125 grids, and the wedge problem on 40×80, 60×120, 80×160 and 100×200 grids. Grid convergence for the bow shock flow has been studied making use of simulations on 20×20, 40×40, 60×60 and 80×80 grids, and the nozzle simulations were performed on 48×16, 72×24, 96×32 and 120×40 grids.

5.4.2 Grid convergence results for flux conservation

The cylindrical expansion flow, the expanding tube flow, the wedge flow and the nozzle flow all have opposed simulation domain boundaries which are ideal walls and thus define a flux tube. We can study grid convergence of the magnetic and momentum flux through these flux tubes. The rotating outflow problem described in the Appendix has the property of radial conservation of magnetic and momentum flux. Fig. 5.8 shows the

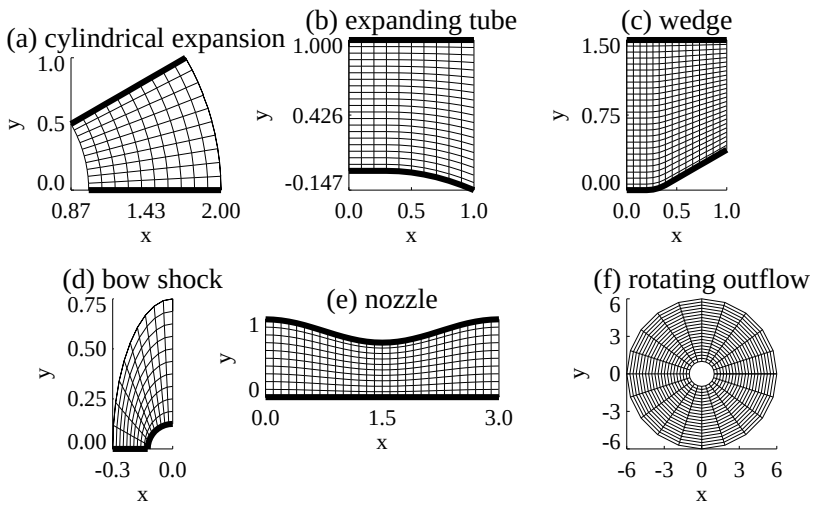

Figure 5.7: *Finite volume simulation grids. Successive conformal refinements of these grids have been used for grid convergence study.*

grid convergence behavior of the fluxes for these five test cases.

The first row of the figure shows the normalized magnetic flux through vertical or radial sections as a function of the vertical or radial coordinate. Every panel contains eight curves, four for the first order scheme (dotted) for increasing grid resolution, and four for the second order scheme (dashed). We see that in all cases the normalized magnetic flux approaches the value of unity nicely, and that the flux conservation is much more accurate for the second order results than for the first order results.

The second row of the figure shows the normalized momentum flux through the vertical or radial sections. Every panel again contains eight curves, four for the first order scheme (dash-dotted) for increasing grid resolution, and four for the second order scheme (dash-dot-dot-dotted). We again see that in all cases the normalized momentum flux approaches the value of unity nicely, and that the flux conservation is much more accurate for the second order results than for the first order results.

The shape of the momentum flux curves is generally similar to the shape of the magnetic flux curves, and this is no surprise for field-aligned flow. Only for the non-field-aligned rotating outflow (Fig. 5.8e) are the curves markedly different in shape.

The third row shows the ten logarithm of the L1 norm of the errors of the magnetic and momentum flux curves, as a function of the grid

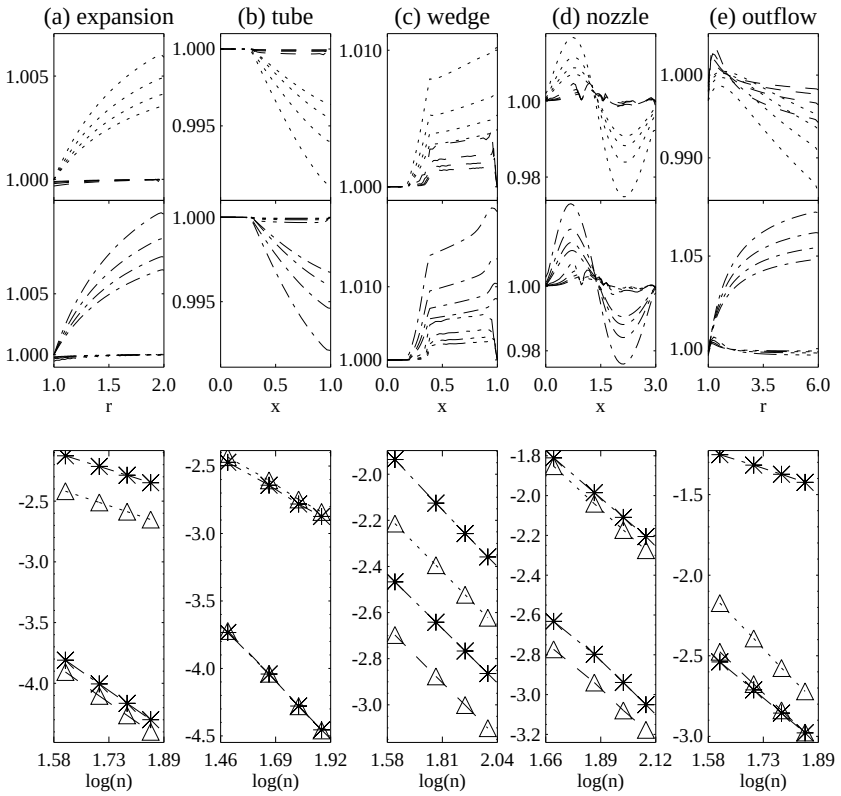

Figure 5.8: *Grid convergence behavior of the magnetic and momentum flux conservation for five test cases. The first row shows the normalized magnetic flux through vertical or radial sections as a function of the vertical or radial coordinate for four different grid resolutions, both for the first order scheme (dotted) and the second order scheme (dashed). The second row shows the normalized momentum flux profiles for the first order scheme (dash-dotted) and the second order scheme (dash-dot-dot-dotted). The third row shows the ten logarithm of the L1 norm of the errors of the magnetic flux (triangles, first order dotted and second order dashed) and momentum flux (asterisks, first order dash-dotted and second order dash-dot-dot-dotted), as a function of the grid resolution (ten logarithm of n, the number of grid cells in the i direction).*

resolution (ten logarithm of n, the number of grid cells in the i direction). The magnetic flux conservation for the first order scheme is indicated by

a dotted line with triangles, and by a dashed line with triangles for the second order scheme. The momentum flux conservation for the first order scheme is indicated by a dash-dotted line with asterisks, and by a dash-dot-dot-dotted line with asterisks for the second order scheme. We observe that in all cases the convergence curves follow a straight line, which indicates convergence with a well-defined order. The fitted slope coefficients for these lines are presented in Table 5.1.

The cylindrical expansion flow and the expanding tube flow are both smooth flows. The fluxes both converge with the expected slope close to -1 for the first order scheme, and close to -2 for the second order scheme. The wedge flow contains a strong discontinuity, and due to the action of the nonlinear limiter, the second order scheme converges only with a slope close to -1, like the first order scheme. The second order results are more accurate, however. The nozzle flow contains shocks as well, and also shows first order convergence both for the first and the second order scheme. The rotating outflow problem is smooth, and shows the expected second order convergence for the second order scheme. For the first order scheme, the momentum flux converges with an order which is lower than first order, but, remarkably, the magnetic flux converges with slope -2.3.

The main conclusions to be drawn from this grid convergence study for magnetic and momentum flux conservation, is that the experimentally obtained grid convergence orders are very close to the theoretically expected orders. The numerical schemes seem thus to behave extremely well. The excellent conservation of magnetic flux indicates strongly that the Powell source term approach to control $\nabla \cdot \vec{B}$ produces valid results.

5.4.3 Grid convergence results for global invariants

Table 5.1 contains the fitted slopes of the grid convergence curves for the global invariants entropy s, stagnation enthalpy h_s, ρ/α and θ. The entropy s is not a global invariant when shocks are present. In the case of the rotating outflow, the invariants are entropy s, Bernoulli function h, angular momentum L and electric field E_z, as discussed in the Appendix. Note that no error slope has been given for the grid convergence of the angle θ between the magnetic and velocity field for the case of the cylindrical expansion. In the initial condition the fields are aligned perfectly up to the machine error induced by a rotation, and this property is conserved throughout the time relaxation as the flow is perfectly radial. These rotational machine errors are very small — much smaller than the errors in the other global RIs — and do of course not depend on resolution, such that for this case grid convergence of θ is not relevant. The *first order scheme* produces grid convergence orders which are generally close to the theoretically expected slope of -1. For some model problems

Table 5.1: *Grid convergence order of several invariant quantities for the model flows discussed in this Chapter. The fitted slope of the ten logarithm of the L1 norm of the error as a function of the ten logarithm of the number of grid cells in the i direction, is shown. For the values marked with an asterisk, the rotating outflow grid convergence is measured using slightly different invariant quantities than for the other flows. The results show that the presence of discontinuities (in the wedge, bow shock, and nozzle flows) consistently degrades the convergence for the second order numerical scheme to first order due to the action of the nonlinear limiter. Analytical singularities or numerical inaccuracies at boundaries and grid distortion may further degrade the convergence. Such additional convergence degradation can be observed for the values that are italicized. Overall, a satisfactorily consistent grid convergence behavior is obtained.*

	expans.	**tube**	**wedge**	**shock**	**nozzle**	**outflow**
1st order						
Φ_B	-0.98	-1.05	-1.04		-1.08	-2.30
Φ_m	-0.93	-1.04	-1.08		-1.01	*-0.72*
s	-0.93	-0.87				-0.81
h_s	-0.82	-1.04	-1.15	-0.86	-0.91	*-0.58**
ρ/α	-0.87	-0.99	-0.97	*-0.72*	*-0.70*	-0.82*
θ		-0.99	-1.06	*-0.60*	*-0.73*	-0.84*
$\nabla \cdot \vec{B}$	-0.98	-0.92	-0.79	-0.59	-0.90	-1.33
F	-1.98	-1.92	-1.79	-1.55	-1.90	-2.36
2nd order						
Φ_B	-2.06	-1.90	-1.03		-1.04	-2.10
Φ_m	-2.06	-1.86	-1.02		-1.07	-1.85
s	-1.96	-1.74				*-1.28*
h_s	-1.91	*-1.10*	-1.01	-0.90	-0.87	-1.92*
ρ/α	-2.07	*-1.44*	-0.82	-1.07	-0.97	-1.71*
θ		-1.78	-0.99	-0.85	-1.01	-1.89*
$\nabla \cdot \vec{B}$	-1.96	-1.38	-0.22	-0.55	-0.42	-1.79
F	-2.95	-2.39	-1.22	-1.53	-1.43	-2.83

and for some invariants, the convergence order is smaller than 1. In

this case the slopes are shown in *italics*, where we have (arbitrarily) put the limit of expected behavior at 80% of the theoretical values. Convergence degradation seems to be most severe for the bow shock and nozzle flows, and detailed study of the simulation results shows that this can mainly be attributed to the interaction of the shocks with the boundaries. Overall, however, the results are quite consistent with the order of the scheme. For the smooth flow problems, the *second order scheme* produces grid convergence orders which are generally close to the theoretically expected slope of -2, except for the values in italics. For the expanding tube flow, careful study shows again that convergence degradation can be attributed to inaccuracies at the (not perfectly smooth) boundary. The model problems with shocks show consistent first order convergence behavior, again due to the limiter.

Table 5.1 also shows grid convergence slopes for $\nabla \cdot \vec{B}$ and Linde's quantity F. For the first order scheme, we see that $\nabla \cdot \vec{B}$ converges with an order not too far from the expected convergence order for state variables, although it is a quantity obtainable from the magnetic field through derivation. The reason may be that the numerical scheme treats $\nabla \cdot \vec{B}/\rho$ as a passive scalar [118]. Linde's quantity F indeed converges one order faster than $\nabla \cdot \vec{B}$. The second order scheme produces satisfactory grid convergence behavior for the $\nabla \cdot \vec{B}$-related quantities as well, except for the wedge, the bow shock and the nozzle. Again the convergence degradation there can be traced back to errors at (not perfectly smooth) boundaries and shock-boundary interactions. Our results on $\nabla \cdot \vec{B}$ convergence for a broad set of model problems confirm the results reported by Linde [99] and Barth [7] for smaller sets of model problems.

To conclude this section about the grid convergence study for global invariants, we can say that the experimentally obtained grid convergence behavior is satisfactorily consistent with the theoretically expected behavior. Some convergence degradation can be observed at (not perfectly smooth) boundaries and shock-boundary interactions, but this is not unexpected, given the discussion on convergence degradation in Sec. 5.3. The fluxes discussed in the previous Section, which can be considered as one-time-integrated quantities, seem to be less sensitive to boundary effects. The results discussed in this Section thus confirm again the validity of the numerical approach and the source term technique to control $\nabla \cdot \vec{B}$.

5.4.4 Grid convergence results for Rankine-Hugoniot relations

For the wedge flow, the inflow quantities and the wedge angle completely determine the angle and the downstream quantities of the fast MHD shock. The algebraic equations of the MHD RH relations 3.75

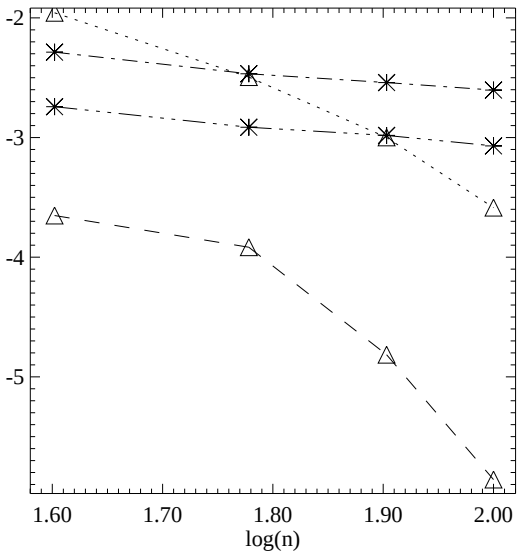

Figure 5.9: *The wedge flow. Grid convergence of the Rankine-Hugoniot relations. Ten logarithm of the relative errors of the downstream density and velocity at* $(x = 0.96, y = 0.87)$*, as a function of the grid resolution. The density (first order scheme, dotted, triangles, and second order scheme, dashed, triangles) does converge, but not with a well-defined order. The velocity converges with* $a = -0.79$ *(first order scheme, dash-dotted, asterisks), and with* $a = -0.80$ *(second order scheme, dash-dot-dot-dotted, asterisks).*

can be solved numerically up to a very high accuracy, using for instance standard iterative methods provided in software for symbolical calculations. Following such a procedure, we have obtained the (nearly) exact downstream density and velocity field magnitude to be $\rho = 2.00060295$ and $v = 7.04956575$. In Fig. 5.9 we investigate grid convergence of the Rankine-Hugoniot relations. The ten logarithm of the relative errors of the downstream density and velocity at $(x = 0.96, y = 0.87)$ is shown, as a function of the grid resolution. First of all we can say that our numerical scheme calculates a solution which closely matches the RH relations. The errors are 1% and lower. The velocity seems to converge linearly with a slope close to the theoretically predicted one, but the density seems to behave more erratically. Fig. 5.10a indicates a reason for this. MUSCL finite volume schemes have the well-known defect that

they produce grid-related entropy oscillations in a direction parallel to a shock, and these entropy errors are advected downstream along the streamlines. This generates small ripples in the downstream solution which should be uniform. The value of the downstream density, for instance, thus depends of the location and on the grid resolution, and this degrades pointwise convergence. The entropy oscillations are quite small with the Lax-Friedrichs scheme, and would be much larger when using the Roe scheme. Due to the inherent defect of finite volume schemes, we can not prove proper grid convergence of the RH relations, but we can see that the RH relations are generally well satisfied, and that the tendency is that they are better satisfied on finer grids. It will be interesting to see [22] if new MHD schemes based on multi-dimensional approaches will reduce or eliminate the downstream entropy contamination typical for finite volume approaches.

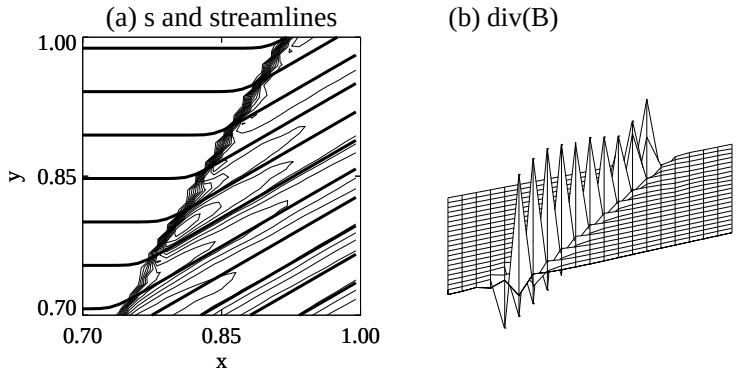

Figure 5.10: *The wedge flow. (a) Entropy contours (15 contours between $s = 2.43$ and $s = 2.45$, thin) and streamlines (thick) in a small region which contains the shock. Small errors in the entropy generated at the shock are convected away downstream parallel to the streamlines, generating small ripples in the downstream region which should be uniform. (b) Divergence of the B field in a small region containing the shock ($x \in [0.6, 0.8]$, $y \in [0.55, 0.75]$). $\nabla \cdot \vec{B}$ is strongly non-zero in a small layer around the shock. Negative and positive $\nabla \cdot \vec{B}$ peaks cancel each other out, such that on a slightly more global scale, magnetic monopoles are not present. $\nabla \cdot \vec{B}$ reaches values from -3.36 to 6.76 in the region shown.*

It is interesting here to investigate more closely what happens with the $\nabla \cdot \vec{B}$ constraint at a strong discontinuity. Fig. 5.10b shows the divergence of the B field in a small region containing the shock ($x \in$

$[0.6, 0.8]$, $y \in [0.55, 0.75]$). $\nabla \cdot \vec{B}$ is strongly non-zero in a small layer around the shock. $\nabla \cdot \vec{B}$ reaches values from -3.36 to 6.76 in the region shown. Actually, an upper bound for $\nabla \cdot \vec{B}$ can be given by $\nabla \cdot \vec{B} = |\Delta B|/\Delta x$, with $|\Delta B|$ the jump in the magnitude of the magnetic field vector across the shock, and Δx a 1D measure of grid spacing. As in the MUSCL schemes discussed above, a stationary shock is generally captured with a constant number of intermediate cells which does not depend on the resolution, and as $|\Delta B|$ is independent of the resolution, this means that $\nabla \cdot \vec{B}$ peaks near shocks grow without bounds as $1/\Delta x$ as a function of the grid resolution. Since second order schemes produce sharper shocks, the $\nabla \cdot \vec{B}$ peaks are larger when using a second order scheme than when using a first order scheme, and our simulation results clearly confirm that (not shown). The Roe scheme, which produces sharper shocks than the Lax-Friedrichs scheme, also produces larger $\nabla \cdot \vec{B}$ peaks at shocks. The Powell source term approach takes into account these $\nabla \cdot \vec{B}$ peaks consistently and the source term precisely neutralizes the dynamical effect of the $\nabla \cdot \vec{B}$ peaks. It is important to note that the exact location and magnitude of the $\nabla \cdot \vec{B}$ peaks changes when a different discretization is chosen for $\nabla \cdot \vec{B}$, and even in numerical schemes which guarantee $\nabla \cdot \vec{B}$ to vanish with machine precision in a certain discretization, it is clear that $\nabla \cdot \vec{B}$ peaks are present as soon as one looks at $\nabla \cdot \vec{B}$ in a different discretization. $\nabla \cdot \vec{B}$ peaks are an unavoidable consequence of our attempt to represent discontinuities on grids with a finite spatial resolution. All this seems to be quite worrisome, given the fact that magnetic monopoles do not exist in nature, but in practice correct results seem to be produced by numerical schemes on discrete grids. How is this possible? As noted by Linde [99], discretization of $\nabla \cdot \vec{B}$ near shocks has a 'telescoping' property, which can be described as follows. Negative and positive $\nabla \cdot \vec{B}$ peaks cancel each other out, such that on a slightly more global scale, magnetic monopoles are not present. This alternation of positive and negative $\nabla \cdot \vec{B}$ peaks can be seen clearly on Fig. 5.10. This is not a proof that the Powell approach produces valid results. A convincing proof of the validity of Powell's source term approach is given by the results of our grid convergence studies. Table 5.1 shows that the measure of flux conservation F converges faster than the state variables, and thus faster than predicted. Fig. 5.9 shows that the numerical solution satisfies the MHD RH relations up to high precision. Most convincingly, Fig. 5.8 shows clearly that the magnetic flux through flux tubes which may contain fast shocks is conserved and that flux conservation converges with the theoretically predicted order.

For the bow shock flow, we can investigate grid convergence of the solution at the stagnation point. On the stagnation streamline, the RH relations lead to an analytical solution for the state variables downstream of the shock, and using the conservation of s and h_s on the stagnation

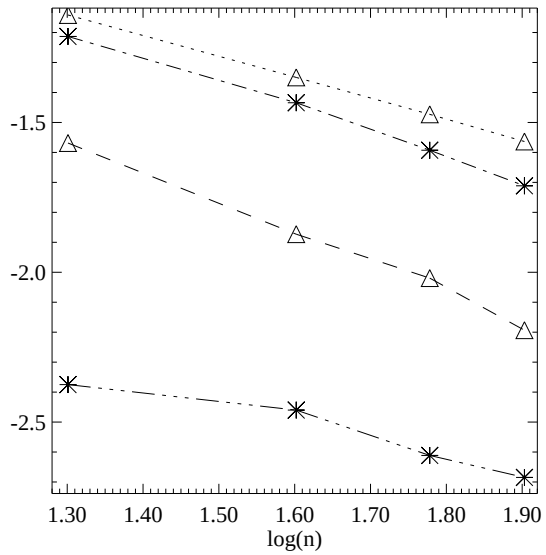

Figure 5.11: *The bow shock flow. Grid convergence of the stagnation point values. Ten logarithm of the relative errors of the stagnation point density and pressure, as a function of the grid resolution. The density converges with* $a = -0.70$ *(first order scheme, dotted, triangles), and with* $a = -1.01$ *(second order scheme, dashed, triangles). The pressure converges with* $a = -0.82$ *(first order scheme, dash-dotted, asterisks), and with* $a = -0.52$ *(second order scheme, dash-dot-dot-dotted, asterisks).*

streamline, the exact analytical solution of the stagnation point quantities in terms of the upstream flow quantities can be obtained [114]. For the inflow values of our bow shock model problem $\rho_{stag} = 3.61528$ and $p_{stag} = 3.61528$. Fig. 5.11 shows grid convergence of the stagnation point values. Although the grid convergence orders are not all close to the theoretical value of one, there is a clear trend of grid convergence to the correct values, and this is a remarkable result, given the well-known problems of many finite volume schemes with 'wall-heating' at perfect walls [91].

5.5 Conclusion

In this Chapter we have studied the grid convergence behavior of our numerical code for six model flows. We did not always obtain grid convergence orders completely consistent with theoretical expectations. Such degradation of convergence can mostly be attributed to analytical singularities or numerical inaccuracies at boundaries, to complex behavior at discontinuities, and to the distortion of the grid. However, in general we *did* obtain satisfactory grid convergence for most properties. The conservation of magnetic and momentum flux in flux tubes behaved especially well (see Table 5.1). All these results give us strong indications that we have calculated the physically correct solution to the flow problems, and that we could improve the accuracy by refining the grid. It is important to establish such formal accuracy tests for MHD simulations, and this is certainly not trivial given the lack of analytical solutions for 2D MHD problems. More advanced schemes and boundary treatment may lead to more completely consistent grid convergence results.

We have investigated by formal grid convergence studies of magnetic flux conservation and other flow quantities, whether the Powell source term approach to control the $\nabla \cdot \vec{B}$ constraint leads to correct results for this class of flows. Our grid convergence results show clearly that this method leads to correct solutions for the transonic problems we considered, although it remains difficult to grasp all the subtle details of how this correct result is obtained. It may also be, that for some problems, for which the conservation of magnetic flux up to very high accuracy is crucial, the source term technique would turn out to be insufficient.

Although the model problems presented in this Chapter exhibit quite a variety of flow features, they all belong to the sub-class of stationary planar 2D MHD flows. Stationary flow has important applications, and in this Chapter we have taken a first important step to prove grid convergence for model problems belonging to this important sub-class of flows. It would certainly be useful to develop more general test problems allowing for grid convergence studies, which, for instance, would also investigate the accuracy of time integration. Self-similar MHD flows are probably good candidates for this. Fully 3D test problems should be considered as well. In 3D, when the magnetic field is not aligned to the flow, many of the invariants used in this Chapter to prove grid convergence, cease to be invariant (Chap. 3), so it is to be expected that it will be more difficult to formulate 3D MHD model flow problems which allow for grid convergence study. For the time being, however, we can reassure ourselves by realizing that many 3D algorithms are straight extensions of their 2D counterparts, so it can be expected that the 3D algorithms perform similarly to the 2D algorithms in terms of accuracy.

Appendix: Radial outflow from a rotating cylindrical object

In this Appendix we describe and analyze a model problem describing radial outflow from a rotating cylindrical object. The grid convergence study for this problem is integrated in the discussion in Sec. 5.4.

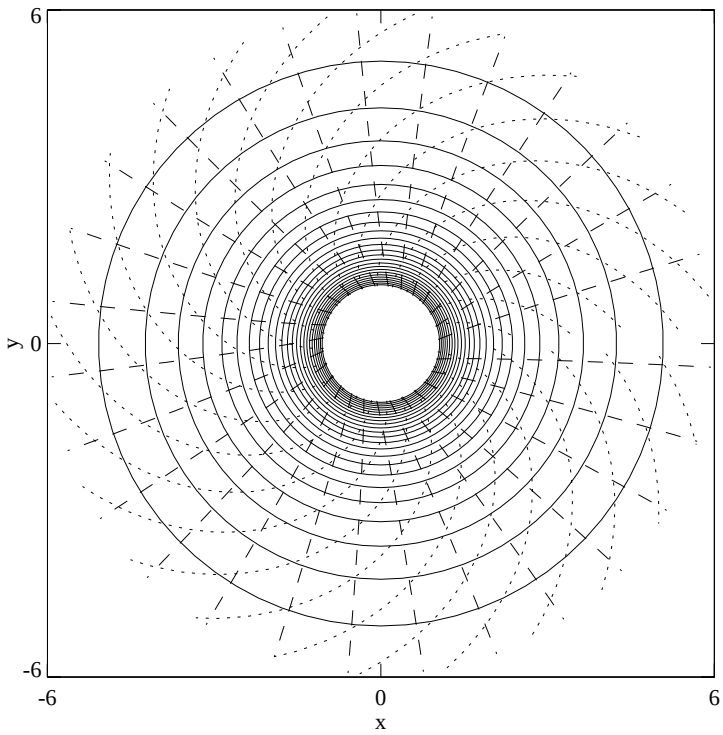

Figure 5.12: *The rotating outflow problem (70 × 70 grid). Density contours (thin solid), streamlines (dashed) and magnetic field lines (dotted) are shown. The magnetic and velocity fields are not aligned. The flow is smooth in the whole simulation domain.*

We start from the cylindrical expansion flow described in Sec. 5.2.1. We take the same inflow conditions and keep $\gamma = 5/3$, but add a rotational velocity component $v_\theta = 1$ in the anti-clockwise direction. The magnetic field remains radial at the boundary $r = 1$. We extend the

simulation domain up to $r = 6$ and $\theta = 360°$. The resulting smooth stationary flow is shown in Fig. 5.12. The magnetic field lines (dotted) are clearly not aligned with the streamlines (dashed). If we transform to a coordinate frame rotating rigidly around the origin with angular velocity $\Omega = -1$, the velocity becomes radial, and thus parallel to the magnetic field (which is not changed by the coordinate transformation). It can be proved that in this rotating frame the magnetic field and the velocity field are aligned everywhere, if they are aligned at the boundary and if the flow is stationary. This is again just a consequence of the MHD frozen-in condition. In the rest frame, however, the flow is not field-aligned, as can be seen in Fig. 5.12. This flow can thus be interpreted as a field-aligned radial outflow from a rotating object, and is related to flows studied in the context of stellar winds [131, 82].

We want to study the grid convergence behavior of this non-field-aligned flow, but cannot directly use the characteristic invariants derived for field-aligned flow. Fortunately, related invariants can be found for this effectively 1D rotating flow [131, 82], as is briefly reviewed next.

The rotating outflow is completely specified when the six constants s, f_m, f_B, Ω, r_A and h are chosen in

$$\begin{aligned} s &= \frac{p}{\rho^\gamma} \\ f_m &= \rho v_r \, r \\ f_B &= B_r r \\ (v_\theta - \Omega \, r) \, B_r - v_r B_\theta &\equiv E_z \equiv 0 \\ \Omega \, r_A^2 = r \left(v_\theta - \frac{B_r B_\theta}{\rho v_r} \right) &\equiv L \\ h = \frac{1}{2} \, v_r^2 + \frac{1}{2} \, (v_\theta - \Omega \, r)^2 + \frac{\gamma}{\gamma - 1} \frac{p}{\rho} - \frac{1}{2} \, \Omega^2 \, r^2. & \end{aligned} \tag{5.6}$$

Here s is the entropy, f_m and f_B are the radial momentum flux and magnetic flux, Ω is the angular speed of the rotating object, r_A is the *Alfvén radius* and h is the *Bernoulli constant*. E_z is the electrical field in the z direction, and L is the angular momentum density. The invariants defined in Eq. (5.6) are used to study grid convergence for the rotating outflow problem in Sec. 5.4.

Following Sakurai [131], we derive the *Bernoulli function* $H(r, \rho)$

$$H(r,\rho) = \frac{f_m^2}{2\rho^2 r^2} + \frac{1}{2} r_A^2 \Omega^2 \left(\frac{r_A/r - r/r_A}{1 - \rho f_B^2 / f_m^2} \right)^2 + \frac{\gamma}{\gamma - 1} s \rho^{\gamma - 1} - \frac{1}{2} \Omega^2 r^2. \tag{5.7}$$

For given constants s, f_m, f_B, Ω and r_A we can implicitly describe the *orbits* $\rho(r)$ as level curves of the Bernoulli function $H(r, \rho) = h$ for varying h. Fig. 5.13 shows these orbits (dotted) for the values of s, f_m,

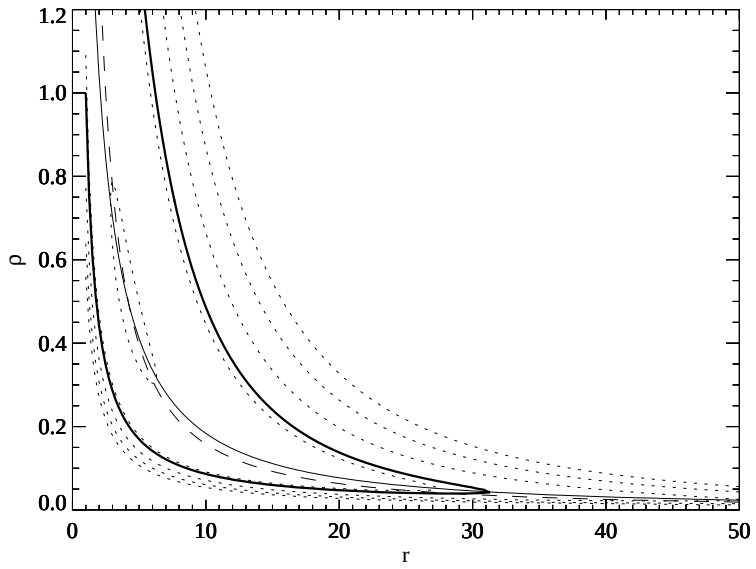

Figure 5.13: *Critical point analysis for the rotating outflow problem. The dotted lines are solution orbits. The thick solid line is the orbit corresponding to the flow shown in Fig. 5.12. The thin solid line is the fast/slow critical curve, and the dashed line is the 'throat' curve. There is one finite critical point (of O-type) where these two curves intersect. The outer radius of the simulation domain has to be chosen smaller than approximately* $r = 30$ *to obtain a continuous stationary solution. Indeed, at the point where the orbit and the fast/slow line cross, the flow becomes subfast. The continuous orbit becomes multi-valued, which means that there is no continuous solution, but a (non-stationary) shock would be formed.*

f_B, Ω and r_A corresponding to the simulation shown in Fig. 5.12. The thick solid orbit corresponds to the value of the Bernoulli constant h of the simulation. Two other curves of interest are the *fast/slow Mach curve* defined by $\partial H/\partial \rho = 0$ (thin solid) and the *throat curve* defined by $\partial H/\partial r = 0$ (dashed). Orbits are vertical where they cross the fast/slow Mach curve, and horizontal where they cross the throat curve. The fast/slow Mach curve and the throat curve cross in an *O-type critical point*. This critical point analysis is instructive because it shows that the outer radius of the simulation domain has to be chosen smaller than approximately $r = 30$ to obtain a continuous stationary solution. Indeed,

at the point where the orbit and the fast/slow line cross, the flow becomes subfast. The continuous orbit becomes multi-valued, which means that there is no continuous solution, but a (non-stationary) shock would be formed. The model problem of Fig. 5.12 does thus not constitute an example of a smooth outflow in an infinite domain. In an appropriately chosen finite domain, however, this problem describes a valid MHD flow with well-defined boundary conditions (the flow remains superfast at the outer boundary), and is thus perfectly suitable for the purpose of testing a numerical MHD code through grid convergence study.

To conclude, we can remark that this non-field-aligned model problem is really a very special case. It could be constructed from the cylindrical expansion flow by rotation because the cylindrical expansion problem has the peculiar property that the flow, the boundary shapes and the boundary conditions themselves are all rotationally invariant. We anticipate that it is very difficult to find stationary 2D non-field-aligned model problems without such special symmetries.